

# Galactic seismology: can the *Gaia* ‘phase spiral’ co-exist with a clumpy, turbulent interstellar medium?

Thor Tepper-García,<sup>1\*</sup> Joss Bland-Hawthorn,<sup>1</sup> Timothy R. Bedding,<sup>1</sup> Christoph Federrath,<sup>2</sup> and Oscar Agertz,<sup>3</sup>

<sup>1</sup>*Sydney Institute for Astronomy, School of Physics, University of Sydney, NSW 2006, Australia*

<sup>2</sup>*Research School of Astronomy and Astrophysics, Australian National University, Canberra, ACT 2611, Australia*

<sup>3</sup>*Lund Observatory, Division of Astrophysics, Department of Physics, Lund University, Box 43, SE-221 00 Lund, Sweden*

Accepted —. Received —; in original form —

## ABSTRACT

The *Gaia* satellite revealed a remarkable spiral pattern (‘phase spiral’, PS) in the  $z - V_z$  phase plane throughout the solar neighbourhood, where  $z$  and  $V_z$  are the displacement and velocity of a star perpendicular to the Galactic plane. As demonstrated by many groups, the kinematic signature reflects the Galactic stellar disc’s response to a dynamical disturbance in the recent past ( $\sim 0.3 - 3$  Gyr). However, previous controlled simulations did not consider the impact of the multi-phase interstellar medium (ISM) on the existence of the PS. This is crucial because it has been suggested that this weak signal is highly susceptible to scattering by small-scale density fluctuations typical of the ISM. This has motivated us to explore the formation and fate of the PS in a high-resolution, N-body/hydrodynamical simulation of an idealised Galaxy analogue bearing a realistic ISM, which interacts impulsively with a massive perturber. In our models, high gas surface densities within the disc encourage vigorous star formation, which in turn couples with the gas via feedback to drive turbulence. We find that the PS is almost non-existent if the ISM has an excess of power on sub-kiloparsec scales compared to longer wavelengths. This can happen in the absence of star formation and feedback when the gas is allowed to cool. In the presence of turbulent gas maintained by stellar feedback, the PS has a patchy spatial distribution and a high degree of intermittency on kiloparsec scales. We anticipate that future studies of the phase-spiral behaviour on all scales will provide crucial information on star-gas dynamics.

**Key words:** Galaxies – stars: kinematics and dynamics – methods: numerical – methods: analytical – software: simulations – hydrodynamics

## 1 INTRODUCTION

An unexpected result from the European Space Agency (ESA) *Gaia* astrometric survey was the detection of an unusual phase-space signature in the local stellar disc (Antoja et al. 2018). In Galactic cylindrical coordinates ( $R, \phi, z$ ), individual stars have velocities ( $V_R, V_\phi, V_z$ ). In a volume element defined by  $(\Delta R, R \Delta \phi, \Delta z) = (\pm 0.1, \pm 0.1, \pm 1)$  kpc<sup>3</sup> centred on the Sun, the *Gaia* team uncovered a coherent spiral pattern in the  $z - V_z$  phase plane, the so-called ‘phase spiral’.

The phase spiral is most evident when each point of the  $z - V_z$  phase plane is represented by either  $\langle V_R \rangle$  or  $\langle V_\phi \rangle$ , averaged over the local volume. Thereafter, Khanna et al. (2019) showed the phase spiral emerges more clearly when encoded by  $\langle L_z \rangle$ ,<sup>1</sup> which measures stellar angular momentum about the Galaxy’s spin axis. This signature is indicative of a system that is settling from a mildly disturbed state to a stationary configuration through the process of phase mixing

(Lynden-Bell 1967). A recent review of the origins of the phase spiral is provided by Hunt & Vasiliev (2025).

Since its discovery, the phase-spiral phenomenon has been extensively studied using both analytic methods (e.g., Binney & Schönrich 2018; Darling & Widrow 2019; Alinder et al. 2023) and numerical simulations (e.g., Laporte et al. 2019; Bland-Hawthorn et al. 2019; Hunt et al. 2021; Asano et al. 2025). In an attempt to bridge the two approaches, Bland-Hawthorn & Tepper-García (2021, henceforth BT21) carried out a high-resolution, N-body simulation ( $N = 10^8$  particles) that closely follows Binney & Schönrich (2018)’s analytic model. Tepper-García, Bland-Hawthorn & Freeman (2022, henceforth TBF22) improved upon this early simulation by adding a gaseous component in the form of a rotationally supported, isothermal, cold disc in vertical hydrostatic equilibrium. Although the last study did not focus on the emergence of the phase spiral, a comparative analysis between the pure N-body simulation and its hydrodynamical extension revealed that the addition of gas, even if ‘inert’ (isothermal, non star-forming), results in significant damping of the vertical perturbation induced onto the disc by a massive external perturber, which is intimately linked to the emergence of the phase spiral.

In the same year, García-Conde et al. (2022) presented an extensive analysis of the emergence and properties of the phase-spiral

\* tepper@physics.usyd.edu.au

<sup>1</sup> The vertical frequency ( $\nu$ ) of stars depends on the vertical amplitude ( $A_z$ ) of the orbit and the guiding centre radius (or  $L_z$ ); the phase spiral is produced because the vertical frequency depends monotonically on the vertical amplitude of the orbit, and is clearer if either dependence ( $A_z$  or  $L_z$ ) is removed.

phenomenon in a synthetic Milky-Way (MW) analogue found in a ‘zoom-in’ cosmological simulation. This study — the first of its kind — showed that phase spirals qualitatively similar to the *Gaia* phase spiral are probably ubiquitous in simulated MW analogues evolved within a full cosmological context, accounting for dynamical, hydrodynamical, and basic astrophysical, baryonic process (e.g., gas cooling and heating, star formation, stellar feedback and enrichment).

Tremaine et al. (2023) demonstrated, using an analytic model, that a phase spiral can be triggered without an external perturbation by the cumulative effect of a large number of stochastic ‘kicks’ on to the disc stars, resulting from a clumpy background made of dark-matter (DM), giant molecular clouds (GMCs), or a combination of these.<sup>2</sup> In a subsequent study, Gilman et al. (2025) argued that DM substructure within the Galaxy’s halo is unlikely to generate a perturbation that is strong enough.

The findings in these recent studies, most notably Tremaine et al. (2023), are intriguing and have motivated us to extend our earlier study (TBF22) on gas-phase evolution in the Galaxy, where we investigate controlled simulations of an idealised MW interacting with a massive perturber with a focus on the emergence and evolution of disc corrugations that are intimately linked to the phase spiral phenomenon. The new models presented here improve upon earlier work in at least three key aspects: 1) by considering the presence of gas that is not inert, but instead is allowed to cool and heat, and to form stars, accounting for their feedback and enrichment, in a way that captures the multi-phase nature of the interstellar medium (ISM) and the clumpy structure of the star-formation process in the Galaxy; 2) by avoiding the complexity of a full cosmological simulation and the obfuscating effect of several interactions; and 3) by considering a full-scale, three dimensional (3D) Galaxy model, accounting for processes such as the disc’s self-gravity and its differential rotation, which have been shown to be crucial in this context (Darling & Widrow 2019; Banik et al. 2022).

This paper is organised as follows. In Sec. 2 we introduce our new simulation suite. The analysis of the simulation outputs is described in Sec. 3, and the results from this analysis are presented in Sec. 4. Our interpretation of the results, their implications and caveats are discussed in Sec. 5. We wrap up with some final thoughts in Sec. 6.

## 2 SETUP

Our working model is built around the paradigm that the dynamical perturbation of the Galaxy’s disc has been primarily driven by the last disc crossing of the Sagittarius (Sgr) dwarf galaxy some 0.5 - 1 Gyr ago (BT21, see also Binney & Schönrich 2018). Within this paradigm, we simulate the response of the stellar disc adopting different Galaxy models and evolution conditions, with a focus in the formation and evolution of the phase spiral (PS).

In all our models, the Galaxy is approximated by a multi-component system consisting of a host dark matter (DM) halo, a pre-assembled stellar bulge, a pre-assembled stellar disc and, if applicable, a gaseous disc. The DM halo, bulge, and stellar disc have masses  $M_{\text{DM}} \approx 1.45 \times 10^{12} M_{\odot}$ ,  $M_{\text{b}} \approx 1.5 \times 10^{10} M_{\odot}$ , and  $M_{\text{d}} \approx 3.4 \times 10^{10} M_{\odot}$ , respectively, sampled with  $2 \times 10^6$ ,  $10^5$ , and  $5 \times 10^7$  particles. The mass of the gas disc, if present, is different for different models (see below). It is worth noting that all galaxy

**Table 1.** Overview of simulations. Common to all is a synthetic Galaxy, approximated by a multi-component system consisting of a host dark matter (DM) halo, a pre-assembled stellar bulge, and a pre-assembled stellar disc. See text for details.

Identifier	$f_{\text{gas}}^a$	Sgr	Remarks
fg00	0.0	Yes	–
fg00_iso	0.2	No	–
fg10_nsf	0.1	Yes	inert, isothermal <sup>b</sup>
fg20_nsf	0.2	Yes	inert, isothermal <sup>c</sup>
fg20_sf	0.2	Yes	star-forming, multi-phase
fg20_sf_iso	0.2	No	star-forming, multi-phase

<sup>a</sup> Initial gas fraction, which decreases over time as a result of the production of stars. The gas is included in the form of an exponential gas disc with a scalelength  $R_{\text{d}} = 6$  kpc in vertical hydrostatic equilibrium. <sup>b,c</sup> The gas is treated with a strict isothermal EoS adopting a temperature  $T = 10^3$  K and  $T = 2 \times 10^3$  K in fg10\_nsf and fg20\_nsf, respectively.

components are reactive (i.e., ‘live’). The Sgr dwarf is approximated by a point-mass with  $M = 2 \times 10^{10} M_{\odot}$  (if applicable).

Initially, the DM halo and the bulge follow roughly a Navarro et al. (1997) profile with a scale radius  $r_{\text{s}} \approx 15$  kpc, and a Hernquist (1990) profile with  $r_{\text{s}} \approx 0.6$  kpc, respectively; the disc has a radial exponential profile with a scale length  $R_{\text{d}} \approx 3$  kpc, and a vertical sech<sup>2</sup> profile with an average scale height  $h_{\text{s}} \approx 0.3$  kpc. The DM halo structure and mass yields a density consistent with the local estimate ( $\rho_{\text{DM}} \approx 0.015 M_{\odot} \text{pc}^{-3}$ ; Guo et al. 2024). This is relevant to a realistic modelling of the total Galactic potential in the solar circle.

Specifically, we consider the following suite of simulation runs (q.v. Tab. 1):

**fg00:** Pure N-body simulation (i.e., no gas), in which the synthetic Galaxy consists of a host DM halo, a stellar bulge and a stellar disc, all reactive and made up of collisionless particles.

**fg10\_nsf:** N-body/hydrodynamical simulation, in which the synthetic Galaxy is identical to fg00, but includes a exponential gas disc with a scalelength<sup>3</sup>  $R_{\text{d}} = 6$  kpc; the gas disc is in vertical hydrostatic equilibrium, with a mass  $M_{\text{gas}} \approx 4 \times 10^9 M_{\odot}$ , corresponding to a gas fraction  $f_{\text{gas}} = 0.1$ , i.e., 10% the total disc mass (stars and gas); the compound system is evolved adopting a strict isothermal equation of state (EoS) adopting a temperature  $T = 10^3$  K; the gas is thus referred to as ‘inert’.

**fg20\_nsf:** Similar to fg10\_nsf, but the gas disc has a mass equal to 20% ( $f_{\text{gas}} = 0.2$ ) of the total disc mass ( $M_{\text{gas}} \approx 9 \times 10^9 M_{\odot}$ ), and a temperature  $T = 2 \times 10^3$  K

**fg20\_sf:** Identical to fg20\_nsf, but the gas is allowed to cool and heat, and to form stars, accounting for their feedback and enrichment.

Finally, we add the following two ‘control’ simulations to our suite:

**fg00\_iso, fg20\_sf\_iso:** Identical to fg00 and fg20\_sf, respectively, but the synthetic Galaxy is evolved in isolation, i.e., there is *no* interaction with the perturber.

The pure N-body simulation (fg00) and its hydrodynamical counterpart (fg10\_nsf) are adopted from our earlier work BT21 and TBF22, respectively. The other models are introduced in this study for the first time.

<sup>2</sup> See Khoperskov et al. (2019) and Grand et al. (2023) for alternative scenarios.

<sup>3</sup> A gas disc with a scalelength twice that of the stellar disc is a common feature of self-consistent dynamical models of the Galaxy (e.g., Binney & Piffl 2015; Bland-Hawthorn & Gerhard 2016). See Tab. 1.

fg20\_sf is regarded as our more ‘realistic’ simulation, and it is the first of its kind to be published. We note that the increased gas fraction in fg20\_sf with respect to fg10\_nsf is necessary in order to trigger the formation of stars from the outset, given that the values of the relevant parameters (notably the star-formation density threshold and efficiency) are fixed based on other constraints (for a discussion see Agertz et al. 2013). Gas fractions in the range 10–20% are consistent with estimates of the total gas mass in the Galactic disc based on dynamical models (Kalberla & Kerp 2009), as well as consistent with the mean, total baryonic mass of  $\sim 10^{12} M_{\odot}$  haloes (Bonnell 2025).

Simulation fg20\_nsf is intended as benchmarks to assess the effect on the disc response in the presence of an increased potential close to the plane (relative to fg10\_nsf), while fg00\_iso and fg20\_nsf\_iso assess the perturbations induced in the disc by dynamical noise. Run fg20\_nsf is motivated by our earlier findings that a stronger disc potential affects the amplitude and lifetime of the vertical corrugations induced in a disc — which are unequivocally linked to the phase-spiral phenomenon — as a result of a direct interaction with a massive satellite (TBF22). Runs fg00\_iso and fg20\_nsf\_iso are motivated by the claims that, even in the absence of an external perturbation, a clumpy environment (be it of baryonic matter or dark matter) may induce perturbations that trigger a phase spiral (Tremaine et al. 2023; Gilman et al. 2025). Note that the gas temperature in fg20\_nsf was higher than fg10\_nsf ( $T = 2 \times 10^3$  K rather than  $10^3$  K), which was imposed by the higher mass of the disc and our requirement that Toomre (1964)’s  $Q$  satisfies  $\min(Q) \sim 1$  which, in turn, is motivated by the desire to have a disc that is reasonably stable against fragmentation from the outset.

It is worth noting that in all models, the pre-assembled stellar disc is sampled with  $5 \times 10^7$  particles, which is significantly higher than the resolution of cosmological (zoom-in) simulations (e.g., García-Conde et al. 2022), at least a factor 10 higher than the corresponding value adopted in most comparable simulations (e.g., Laporte et al. 2019), and only a factor  $\sim 4$  lower than the number of particles in the highest resolution discs simulated to date (e.g., Hunt et al. 2021; Asano et al. 2025). It must be stressed, however, that none of the earlier work — with the notable exception of García-Conde et al. (2022) — accounted for the presence of gas, let alone the effect of gas cooling/heating and star formation processes, as we do here. More details about component masses, particle resolution, etc., for each of our runs are provided in Tab. 1

All simulations were set up and run with our NEXUS framework (Tepper-García et al. 2024).<sup>4</sup> In brief, the initial conditions (ICs) were created with an extended version of the *Action-based Galaxy Modeling Architecture* (AGAMA) stellar-dynamics library (Vasiliev 2019), that allows the treatment of gas components in addition to collisionless components. The ICs were evolved using a modified version of the Adaptive Mesh Refinement (AMR), N-body/hydrodynamical code RAMSES, last described by Teyssier (2002). The gas was treated by adopting either a strict isothermal EoS (fg10\_nsf and fg20\_nsf), or the ‘sub-grid’ galaxy formation module (fg20\_sf and fg20\_sf\_iso) developed by Agertz et al. (2021, q.v.). We kindly refer the reader to Tepper-García et al. (2024) for more details about our NEXUS simulation framework, in particular the treatment of the gas in fg20\_sf and fg20\_sf\_iso.

All models were run for a total simulation timespan of roughly

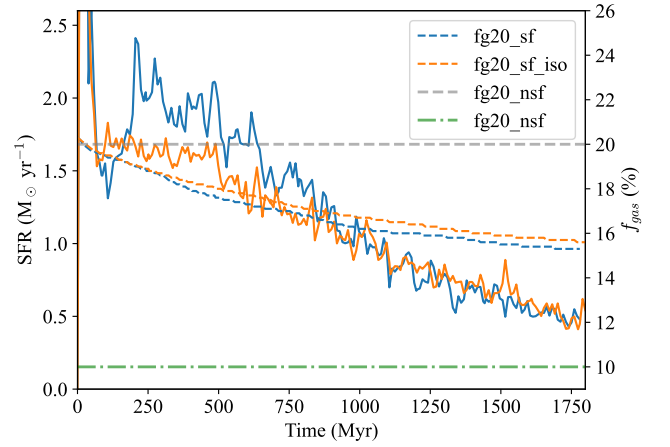


**Figure 1.** Star formation rate (continuous curves; scale on left  $y$ -axis) and total gas fraction (broken curves; scale on right  $y$ -axis) in our hydrodynamical runs. Blue and orange curves correspond, respectively, to the interacting and isolated star-forming Galaxy model. Note that the inert-gas simulations (horizontal grey and green lines) have no star formation and do not experience gas depletion.

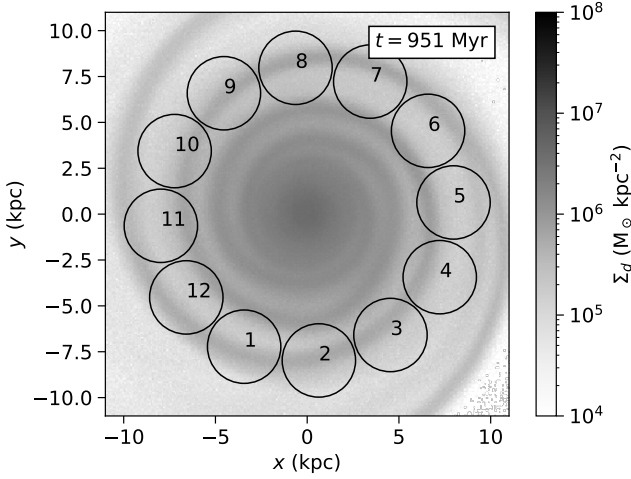
2 Gyr in a cubic box of size 600 kpc per side, adopting a maximum and minimum AMR levels  $l_{\max} = 14$  and  $l_{\min} = 8$ , respectively, implying a limiting spatial resolution of  $\delta x = 600/2^{14} \approx 37$  pc. The Sgr proxy (if included) moved along a hyperbolic orbit which intersects the synthetic Galactic plane *once* at  $R \approx 18$  kpc at  $t \approx 100$  Myr. After the first crossing, the perturber’s mass was exponentially decreased with a time scale of 30 Myr, to reduce its gravitational influence on the disc, thus yielding a clean, one-time impulse onto the synthetic Galaxy. While this is clearly not a realistic approximation of the actual Sgr orbit, it does allow us to study in a transparent fashion the dynamical effect on the stellar disc induced by the single transit of a massive perturber (BT21; TBF22, see also Asano et al. 2025). In addition, as discussed in BT21, we believe that it was Sgr’s last crossing some 0.5 – 1 Gyr ago that triggered the perturbation of the Galaxy’s disc we observe today.

Fig. 1 provides an overview of the star formation history (SFH) and gas depletion in our hydrodynamical runs. The inert gas simulations have no star formation by design, and thus they are not affected by gas depletion. In fg20\_sf and fg20\_sf\_iso, we observe a similar SFH and gas depletion history, although fg20\_sf displays a slight enhanced SFR in the time span  $200 \lesssim t / \text{Myr} \lesssim 1000$ , and a correspondingly higher gas depletion, probably as a result of the interaction with Sgr, but the differences in both quantities with respect to fg20\_sf\_iso are small. Note that the initial star formation ‘burst’ in both runs is a common feature of this type of simulation, where an initially exponential gas disc is allowed to form stars from the outset. A way around this is to evolve the synthetic galaxy under adiabatic conditions for a few hundred million years to allow the disc to settle (effectively, to lose the exponential cusp). However, the long-term evolution is not affected by this (q.v. Bland-Hawthorn et al. 2024).

For ease of discussion, we will refer to the stars already present at the start of the simulation (bulge or disc) as ‘pre-existing’, and to the stars that form out of the gas during the course of the simulation as ‘newly formed’. Note that the latter is adopted regardless of the actual age of the stars. Pre-existing stars are immutable (or inert),

<sup>4</sup> Runs fg00, fg00\_iso, and fg10\_nsf pre-date the publication of our framework, which was however in place by the time we conducted these.





**Figure 2.** Projected stellar density in fg00 at  $t \approx 1$  Gyr. The circles and the inscribed numbers indicate, respectively, the projected sampling volumes and their associated ID along the solar circle ( $R_{\odot} = 8.2$  kpc). Note that the volumes roughly co-rotate with the disc.

i.e., they do not evolve. In contrast, newly formed stars age and lose mass and provide feedback to the environment in the form of energy, momentum, and chemically enriched gas as a result of their evolution. We will focus the remainder of our paper on the kinematic study of the pre-existing disc stars, and will address the newly formed stars in a future study. The reason behind this choice is to allow for a like-for-like comparison between the various simulations, as well as between our study and earlier work, regardless of whether or not star-formation is accounted for.

### 3 ANALYSIS

Our main goal is to study the dynamical perturbation of the Galactic disc by the interaction with Sgr under different sets of conditions, using each of the runs introduced above. Our focus is on the formation and evolution of the phase-spiral phenomenon within the context of a ‘realistic’ Galaxy model that accounts for all the dynamically important components (DM, stars, gas), as well as for the relevant astrophysical processes and components (star formation, turbulence, multi-phase ISM). More specifically, we seek to quantify the incidence rate, i.e., when and where the phase spiral appears during the evolution of each of our synthetic Galaxy models.

To this end, we followed part of the methodology presented in our earlier work (BT21). In brief, we segmented the distribution of pre-existing disc stars around the solar circle ( $R_{\odot} \approx 8.2$ ; GRAVITY Collaboration) with twelve identical, spherical volumes with a diameter of roughly 4 kpc each (see Fig. 2). The volumes are numbered 1 to 12 in an anticlockwise direction. In each volume, we calculated the distribution of stars in vertical phase space  $z - V_z$ , weighted either by azimuthal velocity  $V_{\phi}$ , or by radial velocity,  $V_R$ . We repeated this procedure at different times from start ( $t = 0$  Gyr) to finish ( $t \approx 2$  Gyr) of the simulation, adopting a time step  $\delta t \approx 10$  Myr.

Note that the volumes are fixed into a rotating frame of reference that approximately follows the Galactic rotation (counter-clockwise) at the solar radius; volume 1 is roughly aligned in azimuth with Sgr’s disc crossing location,  $(x, y) \approx (-18, 0)$  kpc, at the impact epoch ( $t \approx 100$  Myr). The intent behind this approach is to sample at all times roughly the same disc region (although not necessarily the same

stars, since these will move in and out of the volume). As discussed in BT21, and found by several independent studies (e.g., Laporte et al. 2019; García-Conde et al. 2022), the precise method used to sample the disc (i.e., co-moving frame vs. fixed frame) does not significantly affect the results.

Note that, prior to calculating the phase space distribution at each time step, the synthetic Galaxy is centred on the centre of mass of the stellar disc using the ‘shrinking sphere’ approach (Power et al. 2003). The angular momentum of the disc is subsequently aligned with the  $z$ -axis of the simulation box. These are both important steps required to properly quantify dynamical quantities.

We visualised the results by arranging the phase-space distribution at each volume along a row, for a given time step, and stack the resulting rows in ascending order of simulation time  $t$ . This yields what we refer to as a phase-space ‘chronogram’. This is a very useful way to visualise the spatiotemporal evolution of the phase spiral, as we have shown earlier (BT21), and it has been adopted by more recent studies (García-Conde et al. 2022; Asano et al. 2025).

This way we end up with two different chronograms: a  $V_{\phi}$ -chronogram, and a  $V_R$ -chronogram, each spanning 12 columns (corresponding to the spherical sampling volumes) and 21 rows (with a time step of roughly 10 Myr, from  $t = 0$  to  $t \approx 2$  Gyr). We refer to each volume-timestep pair on a chronogram as a ‘cell’.

We calculated  $V_{\phi}$ - and  $V_R$ -chronograms for each of our runs, thus allowing for a like-for-like comparison of the incidence rate of the phase spiral across simulations. For the sake of brevity, we do not include examples of chronograms in this study, but instead refer the reader to BT21 (their figure 12), and to the more recent work by García-Conde et al. (2022, their figure 2) and Asano et al. (2025, their figure 12).

#### 3.1 Phase-spiral finder

We seek to identify the epochs and the corresponding locations across the stellar disc (chronogram cells) where the phase spiral is apparent (not necessarily a perfect match to the *Gaia* phase spiral, it must be noted). Rather than performing a visual analysis (cf. Asano et al. 2025), we opted for an automated procedure. To this end, we adopted the approach put forward by García-Conde et al. (2022), who have successfully applied it in the systematic identification of phase spiral in a zoom-in, cosmological simulation.

This method, which is based on the Fourier decomposition of the stellar distribution in vertical phase space, can be summarised as follows: The cell (either of a  $V_{\phi}$ - or a  $V_R$ -chronogram) is partitioned into  $N$  concentric annuli of linearly increasing phase-space radius  $\tilde{R} \equiv (J_z)^{1/2}$ , where  $J_z$  is the vertical action. Next, a Fourier analysis is applied to the distribution of stars within the cell for each annulus, which yields the amplitudes  $A_m$  and phases  $\phi_m$  of modes with  $m = 0$  to  $m = 6$ .

A dipole-like signature is implied by an  $(A_1/A_0)$  profile that is significantly higher than the profiles of the amplitudes of higher modes; a true one-arm spiral signature also requires a monotonically increasing<sup>5</sup> (roughly linearly) phase  $\phi_1$  profile. Similarly, a two-arm spiral is revealed by a dominant  $m = 2$  amplitude and monotonically increasing  $\phi_2$  profile, etc. Henceforth we will concentrate on  $m = 1$  and will defer the analysis of  $m = 2$  modes (cf. Hunt et al. 2022; Asano et al. 2025) to a forthcoming study.

In practice, we deem a dipole-like signal significant if the average

<sup>5</sup> For a spiral wrapping up in a clockwise sense, as is the case of the *Gaia* phase spiral.

value of the  $A_1/A_0$  profile (i.e., the average of  $A_1/A_0$  over  $\tilde{R}$ ) is strictly higher than the average of the other modes, i.e.,  $\langle A_1/A_0 \rangle > \langle A_m/A_0 \rangle$  for  $m = 2, 3, \dots, 6$ . The signal is further considered a strong indication of the presence of a one-arm spiral if the (average) slope,  $\nabla\phi_1$ , of the phase profile over  $\tilde{R}$  (effectively, the slope of a linear fit to the  $\phi_1$  profile) is higher than a given threshold,  $\nabla(\phi)_{\text{th}}$ , and its scatter around a linear fit is below some threshold,  $\sigma(\nabla\phi)_{\text{th}}$ . Following García-Conde et al. (2022), the significance (or ‘strength’) of the signal was estimated by the median value of the  $A_1/A_0$  profile, which we denote as ‘med[ $A_1/A_0$ ]’.

The free parameters of the method, and the values we adopted, are then:  $N = 21$ ,  $\nabla(\phi)_{\text{th}} = 0.1$ , and  $\sigma(\nabla\phi)_{\text{th}} = 0.3$ . We found these values empirically after extensively testing the method with synthetic data (see Appendix A). In general, we found that the method works remarkably well under idealised conditions (see top row in Fig. A1), and it showed satisfactory performance when noise was added to the data (see second to last rows in Fig. A1), which is the case of the data retrieved from our simulations. It is worth noting that the noise induced by the variability in the simulation data is what makes the introduction of  $\nabla(\phi)_{\text{th}}$  and  $\sigma(\nabla\phi)_{\text{th}}$  necessary. Indeed, under ideal conditions,  $\nabla(\phi)_{\text{th}}$  is a constant and  $\sigma(\nabla\phi)_{\text{th}} \equiv 0$  (see top row in Fig. A1).

## 4 RESULTS

### 4.1 Incidence rates across space and time

Applying the phase-spiral finder algorithm introduced above, we transformed each of the  $V_\phi$ - and  $V_R$ -chronograms described in Sec. 3 into an ‘incidence’ map. This is a matrix of  $12 \times 21$  cells, each displaying the value of med[ $A_1/A_0$ ], so that non-empty cells indicate that the corresponding location (column) and time (row) in the synthetic disc hosts a phase spiral. The result of applying this to each simulation yields the set of incidence maps displayed in Fig. 3. To enhance the visual appearance of the maps, we have normalised the detection strength to a maximum value of 4, as indicated by the colour-bar next to each incidence map. Note that there is no obvious quantitative meaning attached to the value of med[ $A_1/A_0$ ]. But since we are not after a match to the *Gaia* phase spiral, our choice has no impact on our analysis; what matters is the differential comparison between the various models.

A few comments preceding the discussion of the results are appropriate. During the testing phase of the phase-spiral finder algorithm, we found that the  $V_R$ - and  $V_\phi$ -incidence maps must be treated differently. This is due to the fact that the range of  $V_R$  extends to both negative and positive values, so the corresponding phase-space map displays both negative and positive values across a roughly symmetric range. In contrast, the  $V_\phi$ -weighted phase-space distribution is always positive, and appears on top of an underlying (background) distribution that is close to a Gaussian, i.e., concentrated at the centre and more diffuse as  $\tilde{R}$  increases. The Fourier decomposition approach appears to work better in the case of the  $V_R$ -weighted maps, so it seems reasonable to apply a suitable transformation to the  $V_\phi$ -weighted maps to obtain a distribution with negative and positive values.

García-Conde et al. (2022) shifted the  $V_\phi$ -weighted map by the mean value  $\langle V_\phi \rangle$  across the map, i.e., effectively displaying the distribution of stars weighted by  $V_\phi - \langle V_\phi \rangle$ . Instead, we normalised the

map by the initial, unperturbed distribution, which is straightforward to get for any of our simulations.<sup>6</sup>

It is worth noting that the method can lead to false positives and false negatives (of order a few percent) but, overall, it generally delivers satisfactory results. We have visually inspected randomly selected volumes in our  $V_R$ - and  $V_\phi$ -incidence maps, and generally confirmed the results of the automated procedure. Therefore, and notwithstanding the caveats of the method, we favour it over a pure visual inspection. That way, all simulations are put on an equal footing, and the comparative analysis is rendered robust against subjectivity.

We now turn to the discussion of the results displayed in Fig. 3, focusing on the  $V_R$ -weighted incidence map (left). The first panel, which corresponds to fg00, a pure N-body model, clearly shows that the phase spiral emerges some 400 Myr after Sgr’s disc crossing (flagged by the horizontal line at the top), but not across all volumes. The signal appears to propagate across a narrow region in azimuth, until it becomes widespread at  $t \approx 750$  Myr (or roughly  $\Delta t \approx 650$  Myr after impact). Thereafter, the presence of the phase spiral becomes more stochastic, fading away with time, and virtually disappearing after  $\Delta t \approx 1150$  Myr. These results show that, in the absence of additional (external) perturbations, the phase spiral is long-lived but eventually vanishes, probably due to the combined effect of phase-mixing and the settling of the disc (TBF22). The need for multiple interactions in order to maintain the phase spiral over long periods is consistent with the results by García-Conde et al. (2022), who found that multiple satellites, even with low mass ( $\leq 10^9 M_\odot$ ), are capable of triggering and sustaining the phase spiral over several billions of years (cf. Laporte et al. 2019; Bland-Hawthorn et al. 2019).

Moving on to the results of fg10\_nsf (second panel from the left in  $V_R$ -weighted incidence map), it is immediately apparent that the emergence of the phase spiral is delayed, and it fades away faster, compared to the first panel (fg00). The difference between fg00 and fg10\_nsf is the presence in the latter of an inert gas disc with a mass equivalent to roughly 10% the total disc mass. Thus, the probable reasons for the difference between the two incidence maps are both the stronger potential close to the plane in fg10\_nsf with respect to fg00 and the dissipative nature of gas, which decrease both the disc’s responsiveness to an impulse perturbation and the time scale for the disc’s settling (TBF22). This is reinforced by the result shown in the third panel (corresponding to fg20\_nsf). In this model, the inert gas disc is twice as massive as in fg10\_nsf, and the phase spiral is mostly suppressed over the entire evolution of the synthetic Galaxy.

Remarkably, when the same, massive gas disc is allowed to cool and heat, and to form stars (i.e., when it is ‘active’ as opposed to inert), the phase spiral becomes apparent again, as demonstrated by the results shown in panel 4 (from the left), corresponding to our most ‘realistic’ simulation (fg20\_sf). Recall that the Galaxy model in this run is initially identical to the model in fg20\_nsf. The phase spiral is less widespread both in space and time compared to fg00 and fg10\_nsf; in fact, it appears rather intermittently, but its presence peaks around the same time as in the other runs ( $t \approx 800$  Myr).

We can consider at least four different explanations for this result. First, the phase spiral is simply triggered by the strong perturbation induced by the merger. This hypothesis can be tested by considering the results shown in the fifth panel (fg20\_sf\_iso). In this model, the gas is forming stars once again but there is *no* interaction with Sgr.

<sup>6</sup> In practice, we chose for this purpose volume = 1, which is statistically equivalent to any other volume.

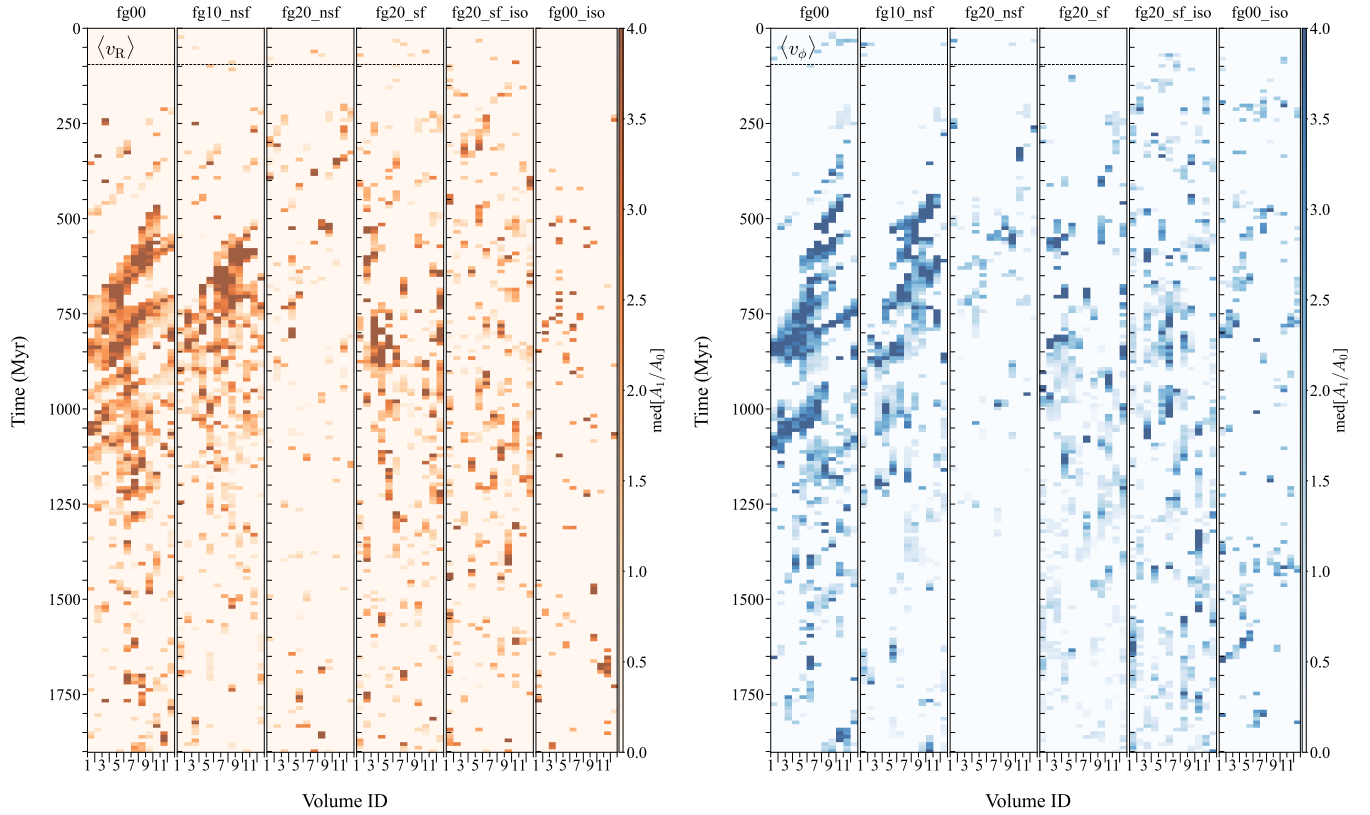


**Figure 3.** Incidence maps, indicating the presence of the phase spiral and its strength (see Sec. 3), weighted by  $V_R$  (left, orange hues) and  $V_\phi$  (right, blue hues), over roughly two billion years of evolution along the solar circle of the synthetic galaxy. For each of  $V_R$  and  $V_\phi$ , each panel corresponds to one of our simulations, as indicated by the panel header (cf. Tab. 1). Within each panel, a cell corresponds to a particular location (column) and time (row) as indicated by the label on the horizontal axis and the vertical axis, respectively. Note that each column corresponds to one of the co-rotating volumes along the solar circle (cf. Fig. 2), and each row to a time step of  $\sim 10$  Myr. The horizontal, dashed line in each panel (if applicable) flags the approximate disc crossing epoch ( $t \sim 100$  Myr). In each map, a darker colour indicates a stronger (i.e., with a higher contrast with respect to the background) phase spiral.

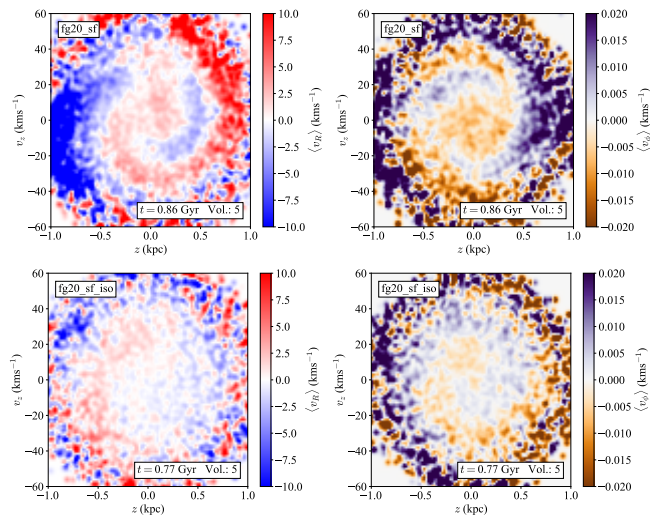


**Figure 4.** Example of phase spirals found in our star-forming, multi-phase gas fg20\_sf (top) and fg20\_sf\_iso (bottom). The corresponding volume and epoch is indicated on the bottom-right corner of each panel. Left: Weighted by  $V_R$ . Right: Weighted by  $V_\phi$ . The bottom panels are examples of phase spirals likely arising from the ‘Tremaine-Frankel-Bovy’ (TFB) effect. Note they are kinematically interlocked – an unexpected result (see main text).

Nevertheless, the incidence map displays isolated pockets of cells where the phase spiral is detected but which appear to be stochastically distributed along the solar circle over the full evolution of the synthetic Galaxy. The incidence rate of the phase spiral is higher than in fg20\_nsf (cf. Fig. 5), but it is not as widespread as in fg20\_sf, probably owing to the absence of an interaction. So, the interaction is one, but not the only, contributor to the appearance of the phase spiral.

Secondly, it could be caused, at least in part, by a decrease in the gas potential as a result of the gas depletion due to star production (cf. Fig. 1). The gas is being replaced by newly formed stars, so there is no net mass loss. But the mass distribution does change, in particular in the direction vertical to the plane. Indeed, the scale height of newly formed stars generally increases with time, which in turn reduces their overall contribution to the potential close to the plane. However, the disc thickening is modest and its effect on the strength of the potential probably small.

The third hypothesis is that the phase spiral is triggered in part by numerical noise. To test this, we show in the last panel of Fig. 3, left, the  $V_R$ -incidence map corresponding to fg00\_iso, i.e., a pure N-body simulation of a synthetic Galaxy evolved in isolation. Clearly, the phase-spiral incidence is extremely low, comparable to the incidence in fg20\_nsf, and significantly lower than fg20\_sf\_iso, which is also evolved in isolation. We conclude that this hypothesis does not seem plausible.

The fourth hypothesis is that the phase spiral in fg20\_sf\_iso (and

partially in fg20\_sf) is triggered by a mechanism similar to that proposed by Tremaine et al. (2023), whereby the cumulative effect of a large number of small, stochastic perturbations imposed onto the stars — perhaps due to the clumpy nature of the ISM — result in the formation of spiral-like structures in phase space. We refer to this as the ‘Tremaine-Frankel-Bovy’ (TFB) effect. Examples of phase spirals found in fg20\_sf and fg20\_sf\_iso are displayed in Fig. 4, in the top and bottom rows, respectively. The latter are probably a result of the TFB effect. It is worth stressing that Tremaine et al. (2023) modelled the evolution of the phase spiral considering purely the density (counts) of stars in phase space as opposed to their distribution weighted by  $V_R$  or  $V_\phi$ . We will return to this point in Sec. 5.

The  $V_\phi$ -incidence maps are displayed on the right in Fig. 3. Qualitatively, we find the same behaviour as in the corresponding  $V_R$ -incidence maps on a simulation by simulation basis. But they are by no means identical, and there are instances where the phase spiral is only detected in one but not the other. We return to this point in Sec. 4.3.

We note a few weak false positives in all runs prior to the disc crossing (indicated by the horizontal dashed line in each panel, if applicable). These are either noise-generated signals, or glitches of the phase-spiral finder algorithm applied to noisy data. Their overall incidence rate and strength can be estimated by looking at panel 6 (from the left); clearly, they are insignificant and can thus be safely ignored.

#### 4.2 Incidence rates over time

Incidence maps provide a detailed view of when and where the phase spiral appears during the evolution of the disc. But given the equivalency<sup>7</sup> in the azimuth along the solar circle — resulting from the initial axisymmetry of our synthetic Galaxy — it seems reasonable to consider the incidence rate in time alone (rather than time *and* space) by marginalising each incidence map over space (effectively summing up over columns). This yields, for each map, the incidence rate of the phase spiral over time.

Fig. 5 displays these for each of our runs, for  $V_R$  (top) and  $V_\phi$  (middle). The vertical dashed line in each panel flags the approximate impact epoch (if applicable). In most cases, we see the general trend — already noted in the previous section — that the incidence rate increases, first slowly and then rapidly, some  $\Delta t \approx 400$  Myr after impact, peaking at around  $t \approx 700 - 800$  Myr, and steadily declining after that.

Intriguingly, there is a significant difference in the temporal incidence — both in  $V_R$  and  $V_\phi$  — between the two unperturbed models (highlighted by a thick black border), with the star-forming, multi-phase gas run (fg20\_sf\_iso) featuring a consistently higher incidence rate at all times compared to its pure N-body counterpart (fg00\_iso).

The bottom panel in Fig. 5 shows the total incidence rate, i.e., over all volumes at all times, for each run split by  $V_R$  and  $V_\phi$ . It is striking that no model displays an incidence rate above 40%, which suggests that the phase-spiral phenomenon is not widespread, at least within our paradigm. It is worth stressing that the rate values are only

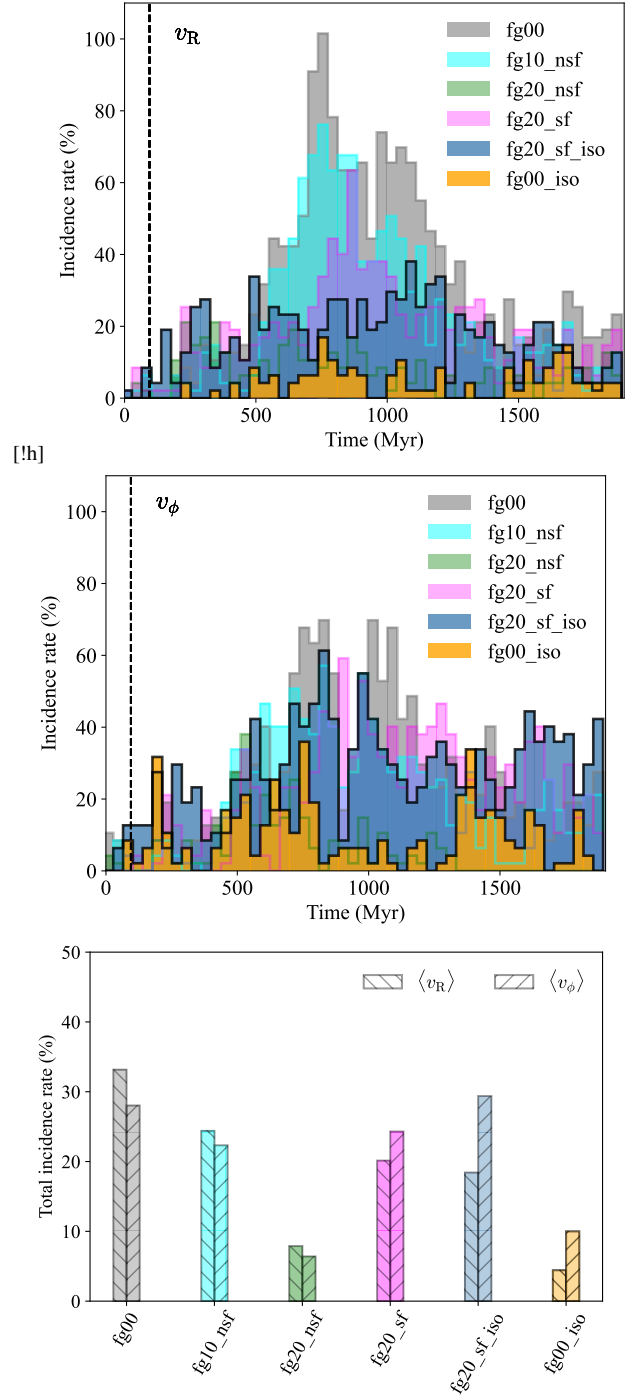


**Figure 5.** Top / Middle: Temporal incidence rate, estimated by marginalising an incidence map over space (i.e., volumes). Results corresponding to the phase spiral weighted by  $V_R$  (top) and  $V_\phi$  (middle) are shown. The vertical dashed line in each panel flags the approximate impact epoch. The distributions of unperturbed runs (fg00\_iso, fg20\_sf\_iso) have been added a black border for emphasis. Bottom: Total incidence rate, across all volumes and over all times.

<sup>7</sup> Locations along the solar circle are strictly speaking not entirely equivalent as a result of Sgr’s disc crossing, but we currently ignore this circumstance which is of minor importance for our analysis.



meaningful in a relative sense, when comparing simulations to one another.<sup>8</sup>

Consistent with the above discussion, the lowest total incidence rates are displayed by the inert, 20% gas fraction run (fg20\_nsf), and the unperturbed, pure N-body run (fg00\_iso), both at less than 10%. The interacting, pure N-body run (fg00) displays the highest total incidence rates at 30 – 35% (the temporal incidence rate is close to 80 – 100% at its highest; see top panel). The total incidence rate of the interacting, pure N-body model is followed by the inert, 10% gas fraction run (fg10\_nsf), which has a comparable total incidence rate to the total incidence rate of our more ‘realistic’ run (fg20\_sf), and its unperturbed counterpart (fg20\_sf\_iso), all in the range 20 – 25%.

### 4.3 Kinematic interlocking

We briefly mentioned in Sec. 4.1 that the  $V_\phi$ -incidence maps and  $V_R$ -incidence maps are qualitatively similar, but not quantitatively similar.

This circumstance is important to consider. The *Gaia* phase spiral is clearly visible not only in star counts (e.g., Laporte et al. 2019), but also when weighing the projected stellar density by  $V_\phi$  or  $V_R$ . As recognised from the outset (Antoja et al. 2018; Binney & Schönrich 2018), this implies that the vertical ( $V_z$ ) and in-plane ( $V_\phi$ ,  $V_R$ ) velocity components of the stars are ‘interlocked.’ Thus, we speak of ‘kinematic interlocking’, a feature that *must* be reproduced, at least qualitatively, by any model attempting to explain the phase-spiral signature.

We looked at the kinematic interlocking in each of our simulations by calculating a ‘coincidence’ map, effectively a cell-by-cell ratio of the  $V_\phi$ - over  $V_R$ -incidence maps, transformed into a ternary signal with a value of 1 for a non-zero, finite ratio lower than 1; a value of 2 for a non-zero, finite ratio higher than 1, and a value of 0 otherwise. The result of this exercise is displayed, for each simulation, in Fig. 6. Black cells indicate cases where the signal in  $V_\phi$  is stronger than in  $V_R$ ; grey cells indicate the opposite. White cells indicate the absence of one or the other in the corresponding incidence map (Fig. 3). The numbers in red at the bottom of each panel indicate the total incidence rates.

Qualitatively, we found the same behaviour as in the individual maps on a simulation-by-simulation basis (Fig. 3), with the difference that the incidence rate of kinematically interlocked phase spirals is notably lower than the individual  $V_R$ - and  $V_\phi$  incidence rates. The pure N-body simulation (fg00) shows the highest incidence rate, followed by fg10\_nsf. In contrast, fg20\_nsf shows virtually no kinematic interlocking, which is hardly surprising, given the very low  $V_\phi$  and  $V_R$  incidence rates. In contrast, and remarkably, the presence of a multi-phase ISM in fg20\_sf\_iso leads to some degree of kinematic interlocking, at a level comparable to fg20\_sf, with the latter having a slightly higher incidence rate; the latter difference is probably driven by the perturbation induced by the satellite.

While the presence of phase spirals in the  $V_\phi$ - and  $V_R$ -incidence maps in the ISM-bearing simulations could be understood in terms of the TFB effect, the latter did not anticipate the corresponding kinematic interlocking.

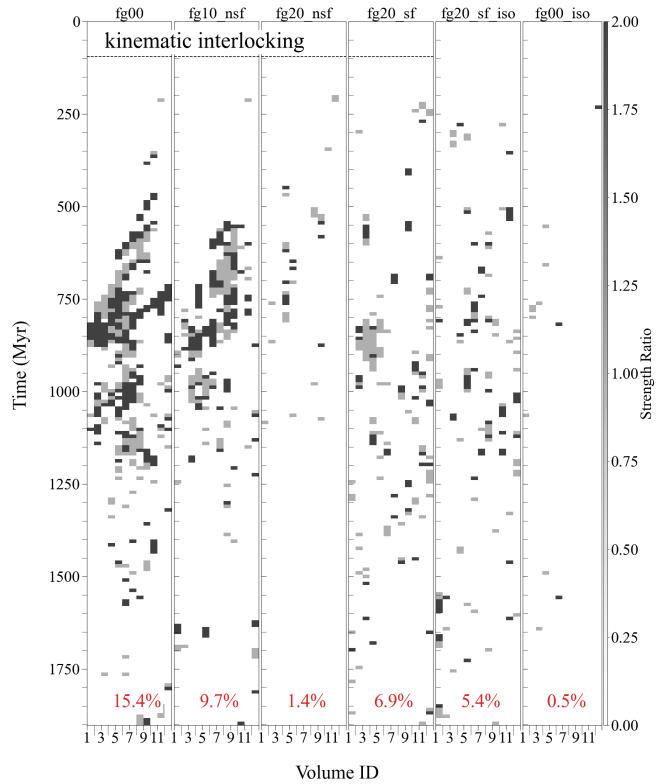


**Figure 6.** phase spiral incidence map, displaying the coincidence of a positive detection in both  $V_R$  and  $V_\phi$ , effectively signalling the presence of a kinematic interlocking between the vertical and in-plane stellar velocity components. The grey scale indicates the ratio of the strength in  $V_\phi$  relative to  $V_R$ : 2 (1) for a non-zero, finite ratio higher (lower) than 1, and 0 otherwise. The numbers (in red) at the bottom of each panel indicate the total incidence rate, i.e., the ratio of the cells with a detection relative to the total number of cells. See text for details.

### 4.4 The effect of the gas structure

The evolved gas disc structure is distinctly different between synthetic galaxies with and without a multiphase ISM, readily apparent to the naked eye, as shown in Fig. 7. Each of the panels in this figure displays the distribution of gas surface densities (PDF) for a different simulation; each histogram corresponds to a specific epoch, as indicated by its colour and the colour palette to the right, which changes from blue hues (‘early’ times) to red hues (‘late’ times). The PDFs were obtained from face-on projections of the 3D gas distribution centred on the disc over an area of  $20 \times 20$  kpc<sup>2</sup>. Each of these projections, or maps, was sampled with  $N_{\text{pix}} = 251$  pixels per side, implying a pixel size of  $\sim 80$  pc, corresponding to roughly twice the limiting, spatial resolution of the AMR grid. In each panel, the initial and the final PDFs are highlighted by a thick green histogram and a thick black histogram, respectively. Note that the initial PDF is identical in all the fg20 models.

The hatched region in each panel of Fig. 7 indicates the range of Jeans (1915) densities, that is, densities prone to fragmentation, which are not resolved in our simulations. The density  $\Sigma_J$  corresponding to a Jeans length  $\lambda_J$  equal to the limiting spatial resolution  $\delta x \approx 37$  pc is calculated by  $\Sigma_J = c_s^2 / G \delta x$ , where  $c_s^2 = k_B T / \mu m_H$  is the sound speed squared,  $k_B$  is Boltzmann’s constant,  $G$  is Newton’s constant,  $\mu$  is

<sup>8</sup> For instance, if the simulations were ran for longer, the rates will probably drop, as the phase spiral will weaken in time, unless there is another interaction or the star-formation is sustained.



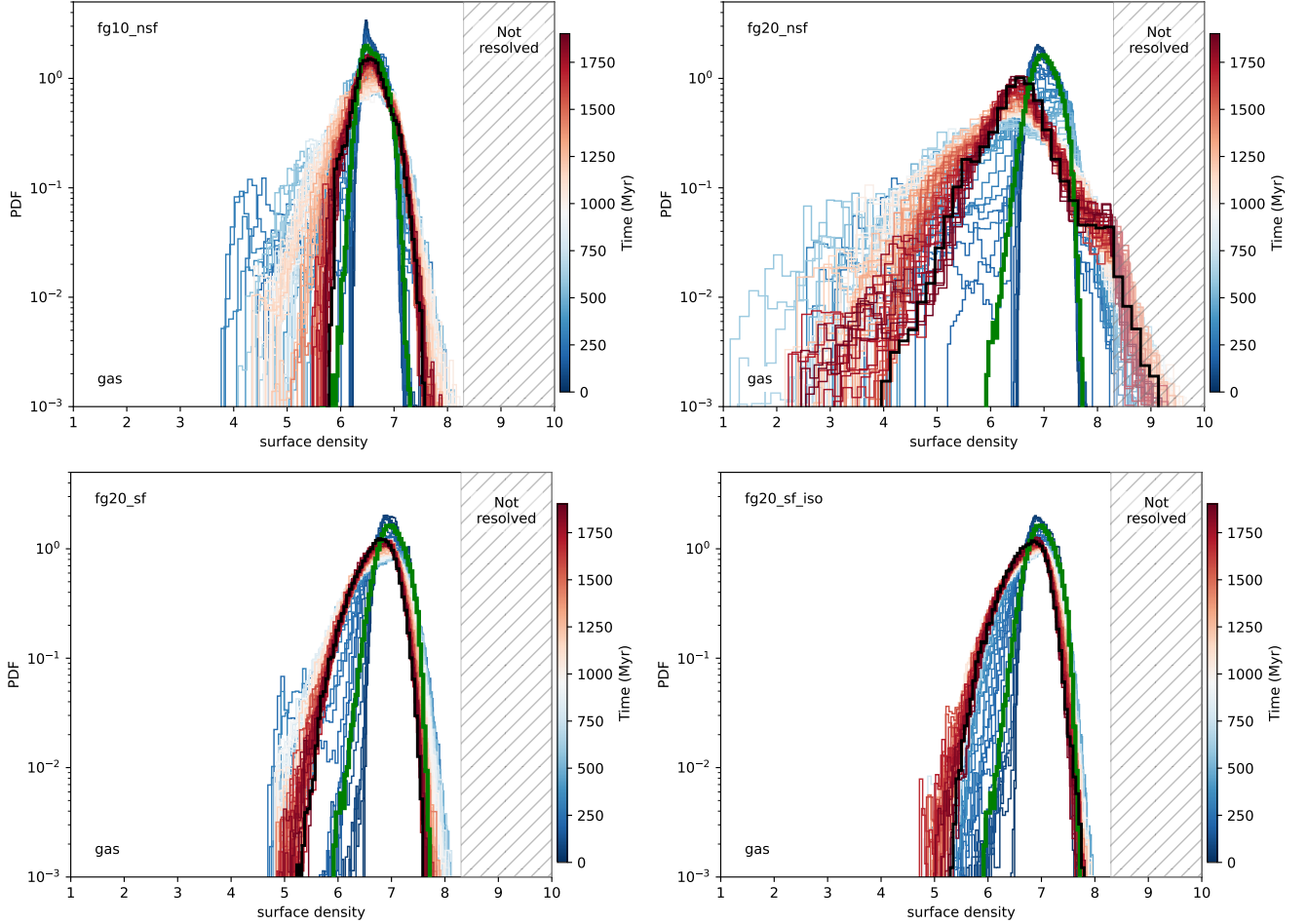


**Figure 7.** Probability distribution of the gas surface density over an area of  $20 \times 20 \text{ kpc}^2$  centred on the disc in different simulations, as indicated by the top-left labels in each panel. In each panel, each curve corresponds to the gas PDF at a given epoch, as indicated by the colour palette. The initial and final states are highlighted by a thick green and a thick black curve, respectively. The hatched region indicates the densities corresponding to the Jeans density at or below the resolution limit of the simulation grid.

the mean molecular weight and  $m_H$  is the hydrogen mass. We adopt<sup>9</sup>  $T = 2 \times 10^4$  and  $\mu \approx 1.22$ , which results in  $\Sigma_J \approx 10^8 \text{ M}_\odot \text{ kpc}^{-3}$ , or twice as high over the pixel scale of the maps.

The heavy, inert, isothermal gas disc (fg20\_nsf; top right panel) shows the most dramatic evolution, from an initially smooth and featureless mass distribution to a highly structured mass distribution that features large-scale, dense filamentary structures; large, dense knots, and large-scale arms after  $\Delta t \approx 2 \text{ Gyr}$  (not shown). These features presumably are the result of a lack of heating, and they would likely become denser, ultimately resulting in a highly fragmented disc, in the absence of a temperature ‘floor’ imposed by the isothermal EoS. The behaviour of the surface density map is reflected in the gas PDF, where an initially narrow distribution spreads out considerably towards both significantly lower and significantly higher densities, reaching into the Jeans density regime.

The active, star-forming, multiphase gas disc (fg20\_sf; bottom-left panel) evolves from the same initially featureless distribution as the disc in fg20\_nsf to one dominated by dense spurs embedded

within pockets of diffuse, hot material, on top of what appears to be a flocculent spiral structure (not shown). The structure appears to be stationary over hundreds of millions of years, sustained by the star-formation activity. As the latter declines, the gas distribution becomes smoother. This evolution results in an extended tail at the lower end of the initial gas PDF. But the evolution of the gas distribution appears to be largely insensitive to the effect of an external perturbation, as suggested by the similarity between the gas PDF in the fg20\_sf and the fg20\_sf\_iso models (bottom panels).

The structure of the light, inert isothermal gas disc (fg10\_nsf; top-left panel) displays an evolution similar to that of the star-forming discs, albeit with a better defined spiral structure (not shown). In consequence, their PDFs experience a similar evolution, although the PDF of the fg10\_nsf model displays an enhancement of lower densities at intermediate times.

For the purpose of a quantitative analysis and comparison of the different gas distributions, we resort to the calculation of the power spectrum of the projected gas density. The use of this mathematical tool is a widely adopted approach to characterise and quantify the structural (and turbulent) properties of the gas distribution in galaxies, not only in observations (e.g., Stanimirovic et al. 1999; Joung & Mac Low 2006; Zhang et al. 2012; Dutta & Bharadwaj 2013), but also in

<sup>9</sup> The initial temperature of the fg20 modes; the initial temperature of the fg10\_nsf model is lower by a factor 2, and so is the corresponding Jeans density but this is irrelevant, since the model never reaches these densities.

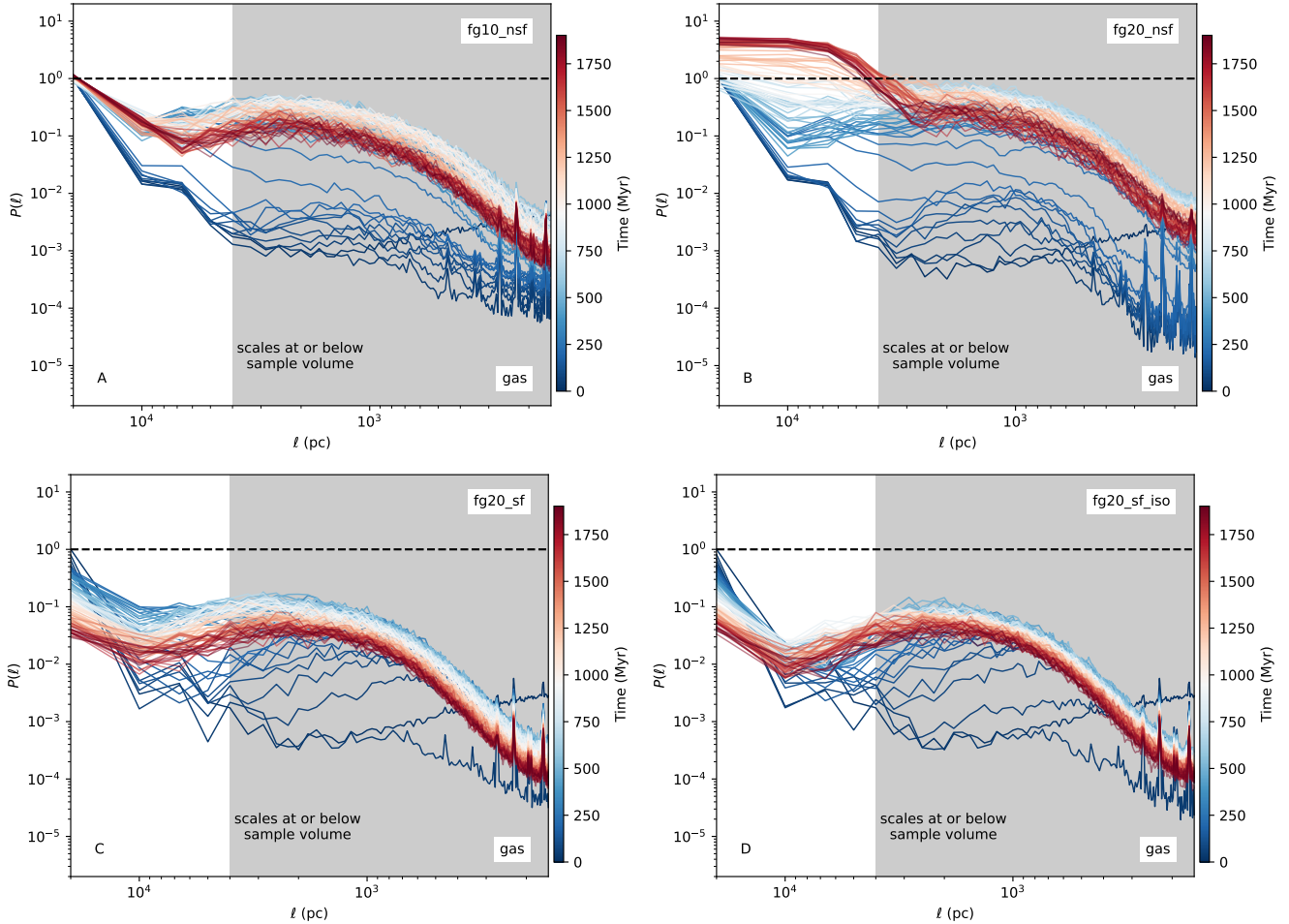


**Figure 8.** Radially averaged power spectrum (RPS) of the surface density distribution of the gas over an area of  $20 \times 20 \text{ kpc}^2$ , normalised to the value of the initial ( $t = 0$ ) power at the largest scale ( $l = 20 \text{ kpc}$ ; the horizontal dashed line is for reference). Each panel corresponds to a simulation, as indicated by the corresponding label on the top-left corner; note that scales decrease from left to right along the  $x$ -axis. In each panel, each curve corresponds to the RPS at a given epoch, as indicated by the colour palette. The shaded area indicates the scales at or below the size of the sample volume (4 kpc), used to analyse the phase spiral (see Fig. 2). The spikes apparent at scales  $l \lesssim 500 \text{ pc}$  are likely artefacts of the discreteness imposed onto the gas distribution by the AMR grid, and they are of no significance. The  $P(l) \propto l^2$  behaviour for  $l \lesssim 1 \text{ kpc}$  displayed by the initial ( $t = 0$ ) RPS in all models is a reflection of the particle noise in the ICs.

simulations (e.g., Bournaud et al. 2010; Grisdale et al. 2017; Renaud et al. 2021).

Here, the power spectrum is calculated by performing a discrete Fast Fourier Transform (FFT) over the ‘raw’ (i.e. without windowing, mirroring, or zero-padding) surface density map and averaging the amplitude over the different spatial frequency ( $k$ ) bins, weighing by the width of the frequency annulus. The radially averaged power spectrum (RPS) thus computed is a measure of the variance of the gas distribution at each spatial scale  $l = 2\pi/k$ . To this end, we adapt the code written and freely provided by Bert Vandenbroucke.<sup>10</sup> We have checked that mirroring, windowing, or zero-padding (cf. Gritton et al. 2017) does not noticeably affect the shape of RPS; any of these manipulations only changes its overall amplitude. Therefore, the conclusions based on the comparative analysis of the RPS performed on the raw maps remain unchanged whether mirroring, windowing, or zero-padding are applied or not.

<sup>10</sup> The results are identical to the results obtained with the Python package *cfpack*, written by C. Federrath, available at <https://www.mso.anu.edu.au/~chfeder/codes/cfpac/cfpac.html>.

We noticed that very high density pixels, i.e. those with values beyond the Jeans density (present only in the *fg20\_nsf* simulation and in relatively low numbers) introduce artefacts in the computed RPS. For this reason, we have reset the density in these pixels to the value of the Jeans density prior to calculating the RPS.

In addition to a spatial analysis, simulations allow for the temporal analysis of the RPS. Thus we calculate the RPS of the gas disc for all gas-bearing models (*fg10\_nsf*, *fg20\_nsf*, *fg20\_sf*, and *fg20\_sf\_iso*) over the full simulation timespan ( $\sim 2 \text{ Gyr}$ ), one for each time step ( $\Delta t \approx 10 \text{ Myr}$ ). The result is displayed in Fig. 8. Each of the four panels (labelled A, B, C, and D, starting from the top-left) corresponds to one simulation, as indicated by the respective top-left legend. In each panel, each curve corresponds to the RPS at a specific epoch, as indicated by the colour palette to the right, which changes from blue hues (‘early’ times) to red hues (‘late’ times). For each RPS, each curve has been normalised to the amplitude of the initial ( $t = 0$ ) power spectrum at the largest scale ( $l = 20 \text{ kpc}$ ); an horizontal dashed line has been included for reference. The grey shaded area indicates the scales at or below the size of the PS sampling volume (see Fig. 2), and it is identical across panels.

In general terms, the amplitude of the RPS in all models increases with time virtually at all scales  $\ell \lesssim 10$  kpc, indicating the emergence of substructure as a result of fragmentation. For reference, the theoretically expected value of the fastest growing modes across the isothermal discs is  $\lambda_{\text{frag}} = 2\lambda_J \approx 0.2 - 1.5$  kpc (it is of order 1 kpc at the solar radius). The growth of the RPS at early time does appear to conform to this expectation in all models.

The light, inert, isothermal disc (fg10\_nsf, panel A) shows little variation at the largest scale, indicating the absence of strong, large-scale coherent structures, although we note that weak spiral arms do appear. In contrast, the RPS of the star-forming discs (panels C, D) display a systematic decrease in amplitude at the largest scale, and a significant increase at smaller scales, indicative of a disc dominated by the appearance of flocculent structure (in accordance with the visual appearance of the surface density maps; not shown). The RPS of the star-forming discs undergo a very similar evolution; therefore, the gas structure does not appear to be significantly affected by the perturbation inflicted on the disc by the satellite.

It is readily apparent that a heavy, inert isothermal gas disc (fg20\_nsf, panel B) displays a distinctively different RPS compared to the other fg20 models within the first billion years of evolution (blue hue curves), in spite of having started from the same state. This is consistent with the visual assessment of the corresponding gas PDFs. Specifically, it displays a rapid increase in the RPS's amplitude at nearly all scales, indicating a strong inhomogeneity in the gas mass distribution.

The difference in the amplitude of the RPS at the relevant scales of  $\lesssim 4$  kpc (corresponding to the size of the sampling volume; see Fig. 2) between the fg20\_nsf model and all the other models is significant, roughly of an order of magnitude. If the amplitude of the RPS is a measure of the gas clumpiness, then these differences may explain the markedly different emergence and evolution of the PS and its incidence rate. In other words, while the presence of a clumpy medium with the right scale may positively affect the PS (TFB effect), it can also stymie the phenomenon if 'too' clumpy.

As shown in Appendix B, the RPS of the other galaxy components (DM, pre-existing stars, or newly formed stars, if present) barely evolves and if so, does in a comparable way across different simulations. This suggests that none of these components significantly impact the onset and evolution of the phase spiral. Thus, the gas and its structure appear to be the key driver of the differences between models in terms of the associated PS incidence rates.

## 5 SUMMARY AND CONCLUSIONS

The key lessons learned from the the incidence maps in Figs. 3 and 6 can be summarised as follows:

- Panels 1, 2, 4: A large-scale perturbation, e.g., an external impulse, is needed to generate a semi-coherent phase-spiral (PS) signal on kpc scales persisting with a lifetime of order 100 Myr.
- Panels 2, 3: Adding inert gas to the disc suppresses the PS signature; the suppression appears correlated with the amount of gas.
- Panels 4, 5: Multi-phase, turbulent gas can sustain, and even trigger, localised PS signatures. We associate this with the TFB effect. Unexpectedly, the PS signatures can even be interlocked, which may be a property arising from the (turbulent) gas motions.
- Panel 6: A measure of the rate of false positives can be seen in the dry isolated disc. These isolated PS signatures are never interlocked and are noisy artefacts.
- Panels 2, 3, 4, 5: The power spectra corresponding to panels 2, 4 and 5 (panels A, C, and D in Fig. 8, respectively) are qualitatively

similar. The power spectrum for panel 3 (panel B in Fig. 8) has roughly an order magnitude more power on the relevant scales  $\lesssim 4$  kpc. This small-scale power appears to totally suppress the PS signal (panel 3).

The upshot is that the phase spiral is influenced by both the quantity and the spatial distribution of gas. Based on our earlier work (TBF22), we know that the amount of gas is key because of the resulting increased potential close to the galactic plane, which affects the stars' dynamics in two ways: 1) by dampening the disc's response to a perturbation; 2) by speeding up the phase-mixing process; both of which negatively impact the PS phenomenon. The power-spectrum analysis indicates that is not only the quantity of gas but also its structure, which both play a role in shaping the phase spiral. Crucially, the influence of newly formed and pre-existing stars is of lesser importance compared to the gas.

These findings are entirely consistent with the result that, without feedback driving, large-scale gas density power spectra have too much power on small scales, which is not compatible with observations (Grisdale et al. 2017). But most importantly, they harmonise with the suggestion that the phase spiral is highly susceptible to scattering by small-scale density fluctuations (TFB effect).

In this context, an unexpected and important result in our study is that clumpy, turbulent gas is capable of triggering *kinematically interlocked* phase-spiral signatures. This result suggests that the phase spiral can, in principle, be used to *probe the ISM's turbulent structure as well as the interplay between the stars and the ISM on  $\sim 100$  Myr timescales*, thus meriting further investigation.

## 6 CLOSING REMARKS

Our simulations hint that the *Gaia* phase spiral *can* coexist with a clumpy, turbulent ISM. *But* the signature is highly intermittent *both* spatially and temporally: there is not a single epoch at which the phase spiral is observable simultaneously across the solar circle, nor is there a specific location across the solar circle where it is observable at all times; this is in contrast to the findings of billion-particle, pure N-body models (Hunt et al. 2021; Asano et al. 2025). We should not be surprised by this. Essentially, all phenomena associated with the ISM are intermittent and stochastic by nature (Seta & McClure-Griffiths 2025), including molecular cloud formation and star formation (Federrath & Klessen 2012), as well as nuclear activity, disc-halo gas recycling, and transient spiral arms, to name a few.

Given that we observe the phase spiral not only in the solar neighbourhood (Antoja et al. 2018), but also beyond (Xu et al. 2020), what can we learn from its spatiotemporal intermittency? Taken at face value, our results imply that the phase spiral is not observable at the present epoch all along the solar circle, nor will it be observable here for all time to come.

But we do need to consider the possibility that the models are incomplete (i.e., lacking relevant physical ingredients) or inaccurate (e.g., because of an inadequate resolution). Clearly, any simulation may benefit from increased resolution in terms of both the particle number and the spatial scale. While an increased spatial resolution may be attainable, billion-particle N-body/hydrodynamical simulations are out of reach for the time being. An increased particle resolution may reconcile, at least in part, the very different behaviour between our simulations and billion-particle simulations with regards to the difference in the spatiotemporal appearance of the phenomenon, i.e. intermittent vs. continuous.

Similarly, we anticipate that consideration of additional relevant physical processes such as magnetic fields and highly energetic

particle (‘cosmic ray’) heating, which are expected to reduce the gap between model galaxies and real galaxies, will have a noticeable effect on the interplay between gas and ISM. There is a long list of studies that have shown how the presence of an even weak magnetic field can significantly affect the density and turbulence structure of the ISM (q.v. [Molina et al. 2012](#); [Banda-Barragán et al. 2018](#); [Beattie et al. 2023](#)). Similarly, cosmic rays resulting from stellar activity are known to modify the temperature of gas (e.g., [Booth et al. 2013](#)), which in turn affect its density structure.

Despite these caveats, our simulations underline the importance of gas in any study aiming at understanding the dynamical response of stellar discs and the consequent wave phenomena associated with, such as the phase spiral. Conversely, the properties (e.g. strength, distribution, interlocking) of the phase-spiral are providing us with information on the strength of small-scale, star-gas coupling in the ISM.

Crucially, results obtained from the analysis ‘dry’ models, i.e., models that do not include gas,<sup>11</sup> may be misleading, because the disc’s response appears to be exaggerated – dry models are simply too ‘reactive.’ We have found this to be true in the context of disc corrugations ([TBF22](#)), and now again in the context of the phase spiral. While dry models can still be useful for exploring certain phenomena under specific conditions, incorporating a dissipative component is generally essential for a comprehensive dynamical study of galactic discs.

## ACKNOWLEDGMENTS

TTG acknowledges financial support from the Australian Research Council (ARC) through Australian Laureate Fellowships awarded to JBH (FL140100278) and to TRB (FL220100117) from the School of Physics, University of Sydney, and for partial funding through the James Arthur Pollock memorial fund awarded to the School of Physics, University of Sydney. We acknowledge the facilities, and the scientific and technical assistance of the National Computational Infrastructure (NCI), which is supported by the Australian Government, through an NCMAS grant (project IDs: ca64 and ek9).

We made use of PYNBODY<sup>12</sup> – a PYTHON<sup>13</sup>-based software – in our analysis for this paper ([Pontzen et al. 2013](#)). This research has made use of NASA’s Astrophysics Data System (ADS) Bibliographic Services<sup>14</sup>.

## DATA AVAILABILITY

The data underlying this article will be shared on reasonable request to the corresponding author.

## References

- Agertz O., Kravtsov A. V., Leitner S. N., Gnedin N. Y., 2013, *ApJ*, **770**, 25  
 Agertz O., et al., 2021, *MNRAS*, **503**, 5826  
 Alinder S., McMillan P. J., Bensby T., 2023, *A&A*, **678**, A46  
 Antoja T., et al., 2018, *Nature*, **561**, 360  
 Asano T., Fujii M. S., Baba J., Portegies Zwart S., Bédorf J., 2025, *arXiv e-prints*, p. [arXiv:2501.12436](#)  
 Banda-Barragán W. E., Federrath C., Crocker R. M., Bicknell G. V., 2018, *MNRAS*, **473**, 3454  
 Banik U., Weinberg M. D., van den Bosch F. C., 2022, *ApJ*, **935**, 135  
 Beattie J. R., Federrath C., Kriel N., Mocz P., Seta A., 2023, *MNRAS*, **524**, 3201  
 Binney J., Piffl T., 2015, *MNRAS*, **454**, 3653  
 Binney J., Schönrich R., 2018, *MNRAS*, **481**, 1501  
 Bland-Hawthorn J., Gerhard O., 2016, *Annual Review of Astronomy and Astrophysics*, **54**, 529  
 Bland-Hawthorn J., Tepper-García T., 2021, *MNRAS*, **504**, 3168  
 Bland-Hawthorn J., et al., 2019, *MNRAS*, **486**, 1167  
 Bland-Hawthorn J., Tepper-García T., Agertz O., Federrath C., 2024, *ApJ*, **968**, 86  
 Bonnell I. A., 2025, *MNRAS*, **540**, L1  
 Booth C. M., Agertz O., Kravtsov A. V., Gnedin N. Y., 2013, *ApJ*, **777**, L16  
 Bournaud F., Elmegreen B. G., Teyssier R., Block D. L., Puerari I., 2010, *MNRAS*, **409**, 1088  
 Darling K., Widrow L. M., 2019, *MNRAS*, **484**, 1050  
 Dutta P., Bharadwaj S., 2013, *MNRAS*, **436**, L49  
 Federrath C., Klessen R. S., 2012, *ApJ*, **761**, 156  
 GRAVITY Collaboration et al., 2019, *A&A*, **625**, L10  
 García-Conde B., Roca-Fàbrega S., Antoja T., Ramos P., Valenzuela O., 2022, *MNRAS*, **510**, 154  
 Gilman D., Bovy J., Frankel N., Benson A., 2025, *ApJ*, **980**, 24  
 Grand R. J. J., Pakmor R., Fragkoudi F., Gómez F. A., Trick W., Simpson C. M., van de Voort F., Bieri R., 2023, *MNRAS*, **524**, 801  
 Grisdale K., Agertz O., Romeo A. B., Renaud F., Read J. I., 2017, *MNRAS*, **466**, 1093  
 Gritton J. A., Shelton R. L., Galyardt J. E., 2017, *ApJ*, **842**, 102  
 Guo R., Li Z.-Y., Shen J., Mao S., Liu C., 2024, *ApJ*, **960**, 133  
 Hernquist L., 1990, *ApJ*, **356**, 359  
 Hunt J. A. S., Vasiliev E., 2025, *arXiv e-prints*, p. [arXiv:2501.04075](#)  
 Hunt J. A. S., Stelea I. A., Johnston K. V., Gandhi S. S., Laporte C. F. P., Bédorf J., 2021, *MNRAS*, **508**, 1459  
 Hunt J. A. S., Price-Whelan A. M., Johnston K. V., Darragh-Ford E., 2022, *MNRAS*, **516**, L7  
 Jeans J. H., 1915, *MNRAS*, **76**, 70  
 Joung M. K. R., Mac Low M.-M., 2006, *ApJ*, **653**, 1266  
 Kalberla P. M. W., Kerp J., 2009, *ARA&A*, **47**, 27  
 Khanna S., et al., 2019, *MNRAS*, **489**, 4962  
 Khoperskov S., Di Matteo P., Gerhard O., Katz D., Haywood M., Combes F., Berczik P., Gomez A., 2019, *A&A*, **622**, L6  
 Laporte C. F. P., Minchev I., Johnston K. V., Gómez F. A., 2019, *MNRAS*, **485**, 3134  
 Lynden-Bell D., 1967, *MNRAS*, **136**, 101  
 Molina F. Z., Glover S. C. O., Federrath C., Klessen R. S., 2012, *MNRAS*, **423**, 2680  
 Navarro J. F., Frenk C. S., White S. D. M., 1997, *ApJ*, **490**, 493  
 Pontzen A., Roškar R., Stinson G., Woods R., 2013, pynbody: N-Body/SPH analysis for python, Astrophysics Source Code Library (ascl:1305.002)  
 Power C., Navarro J. F., Jenkins A., Frenk C. S., White S. D. M., Springel V., Stadel J., Quinn T., 2003, *MNRAS*, **338**, 14  
 Renaud F., Romeo A. B., Agertz O., 2021, *MNRAS*, **508**, 352  
 Seta A., McClure-Griffiths N. M., 2025, *MNRAS*,  
 Stanimirovic S., Staveley-Smith L., Dickey J. M., Sault R. J., Snowden S. L., 1999, *MNRAS*, **302**, 417  
 Tepper-García T., Bland-Hawthorn J., Freeman K., 2022, *MNRAS*, **515**, 5951  
 Tepper-García T., Bland-Hawthorn J., Vasiliev E., Agertz O., Teyssier R., Federrath C., 2024, *MNRAS*,  
 Teyssier R., 2002, *A&A*, **385**, 337  
 Toomre A., 1964, *ApJ*, **139**, 1217  
 Tremaine S., Frankel N., Bovy J., 2023, *MNRAS*, **521**, 114  
 Vasiliev E., 2019, *MNRAS*, **482**, 1525  
 Xu Y., et al., 2020, *ApJ*, **905**, 6  
 Zhang H.-X., Hunter D. A., Elmegreen B. G., 2012, *ApJ*, **754**, 29

<sup>11</sup> We refer to these as ‘dynamical’ models.

<sup>12</sup> <https://github.com/pynbody/pynbody>

<sup>13</sup> <http://www.python.org>

<sup>14</sup> <http://adsabs.harvard.edu>



## APPENDIX A: VALIDATION OF THE PHASE-SPIRAL FINDER

We have conducted an extensive validation of the phase-space finder algorithm described in Sec. 3. To this end, we have created a synthetic phase spiral model, as follows. We create a rectangular grid of in Cartesian coordinates  $(X, Y)$  with  $M \times M$  points. On this grid, the amplitude  $A(X, Y)$  of the phase spiral of mode  $m$  (i.e.,  $m$ -arm), winding  $w$ , and phase shift  $\psi_0$ , centred at  $(X_c, Y_c)$  is given by the following:

$$X' = X - X_c \quad (\text{A1})$$

$$Y' = Y - Y_c \quad (\text{A2})$$

$$\theta = \arctan(Y'/X') \quad (\text{A3})$$

$$r^2 = X'^2 + Y'^2 \quad (\text{A4})$$

$$\psi = \psi_0 + m \theta + w r \quad (\text{A5})$$

$$A_{\text{PS}} = \mathcal{A}_0 \cos[\psi] \quad (\text{A6})$$

For a more realistic model, we optionally add noise described by a Gaussian (normal) distribution  $N(\mu, \sigma)$ , with zero mean  $\mu \equiv 0$  and standard deviation  $\sigma$  equal to the desired noise level. Note that the noise amplitude is chosen relative to the model's. With the above definitions, the full expression for the phase-spiral amplitude is thus

$$AA_{\text{PS}}(X, Y, \sigma) = \mathcal{A}_0 \{ \cos[\psi] + N(0, \sigma) \} . \quad (\text{A7})$$

We have tested the finder using a large number of values picked from reasonable ranges for the phase-spiral model parameters: centre, phase shift, and winding, as well as noise levels, focusing for now on one-arm spirals ( $m = 1$ ) with  $\mathcal{A}_0 = 1$ , and fixing  $M = 100$  (the same resolution used in our phase-spiral incidence-map cells). Via a trial-and-error approach we have been able to tune the free parameters of the phase-spiral finder algorithm to yield satisfactory results in the overwhelmingly majority of cases. In fact, the algorithm works flawlessly in idealised case of no noise ( $\sigma = 0$ ). Overall it works remarkably well up to  $\sigma \approx 20$  in the overwhelmingly majority of cases we've tested for.

An example of such a test case is displayed in Fig. A1. The left column shows a series of examples of synthetic, one-arm ( $m = 1$ ) phase spirals with  $w = 1$  and  $\psi_0 = 0$ , and increasing levels of noise, from  $\sigma = 0$  (top) to  $\sigma = 20$  (bottom), on a  $M = 100$  grid. The middle and right columns show, respectively, the amplitude  $A_m/A_0$  of the Fourier modes  $m = 1, 2, \dots, 6$  and their phase  $\phi$ , as a function of radial bin  $r$  (see definitions above).

Regardless of the noise level, it is clear that: 1) the  $m = 1$  mode amplitude significantly dominates over all the other modes, but the difference decreases with noise level; 2) the  $m = 1$  mode's phase increases linearly with radius, but the scatter around a perfect linear behaviour increases with noise level. In stark contrast, the phase of all the other modes varies erratically (with exception perhaps of  $m = 3$ ). It is striking that even in the  $\sigma = 20$  case (bottom row), where the phase spiral is nearly invisible to the eye, the phase-spiral finder is able to pick up the signal.

Our extensive test suite demonstrated that a dominant  $m = 1$  amplitude throughout and a (ideally) linearly increasing  $m = 1$  phase are necessary and sufficient conditions to detect the presence of a structure reminiscent one-arm spiral.

## APPENDIX B: MASS DISTRIBUTION AND RADIALLY AVERAGED POWER SPECTRUM (RPS)

Here we show the evolution of the RPS of additional galaxy components: pre-existing stars (Fig. B1); dark matter (Fig. B2); and newly

formed stars (Fig. B3). For details about the RPS, we refer the reader to Sec. 5. The key point to take away from these plots is the lack of power on sub-kiloparsec scales compared to Fig. 8. The substructure within these evolving spatial components is neither able to excite nor able to dampen the phase spiral (Tremaine et al. 2023; Gilman et al. 2025).

This paper has been typeset from a  $\text{\LaTeX}$  file prepared by the author.

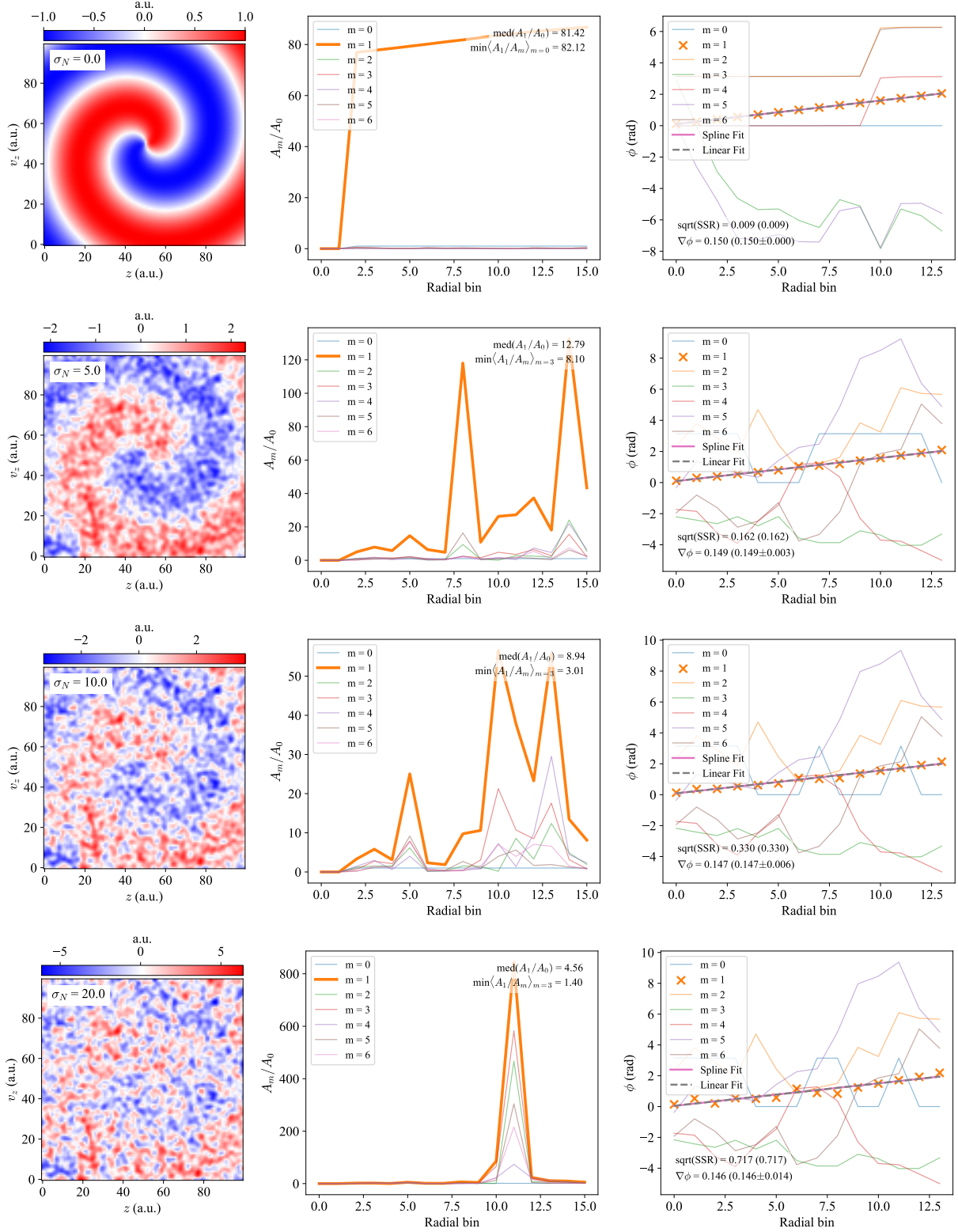


**Figure A1.** Synthetic, idealised phase spiral models. Each rows correspond to the same model, but with a progressively increasing amplitude of Gaussian noise. The left column shows a series of examples of synthetic, one-arm ( $m = 1$ ) phase spirals with  $w = 1$  and  $\psi_0 = 0$ . The red-white-blue colour scheme indicates the value of the phase spiral amplitude  $A_{ps}$ . Note that the axes units and the units of the amplitude are fully arbitrary. The middle and right columns show, respectively, the amplitude  $A_m/A_0$  of the Fourier modes  $m = 1, 2, \dots, 6$  and their corresponding phase  $\phi$ , as a function of radial bin. The results corresponding to the  $m = 1$  mode have been highlighted with a thick, orange curve (middle) and crosses (right), for emphasis.

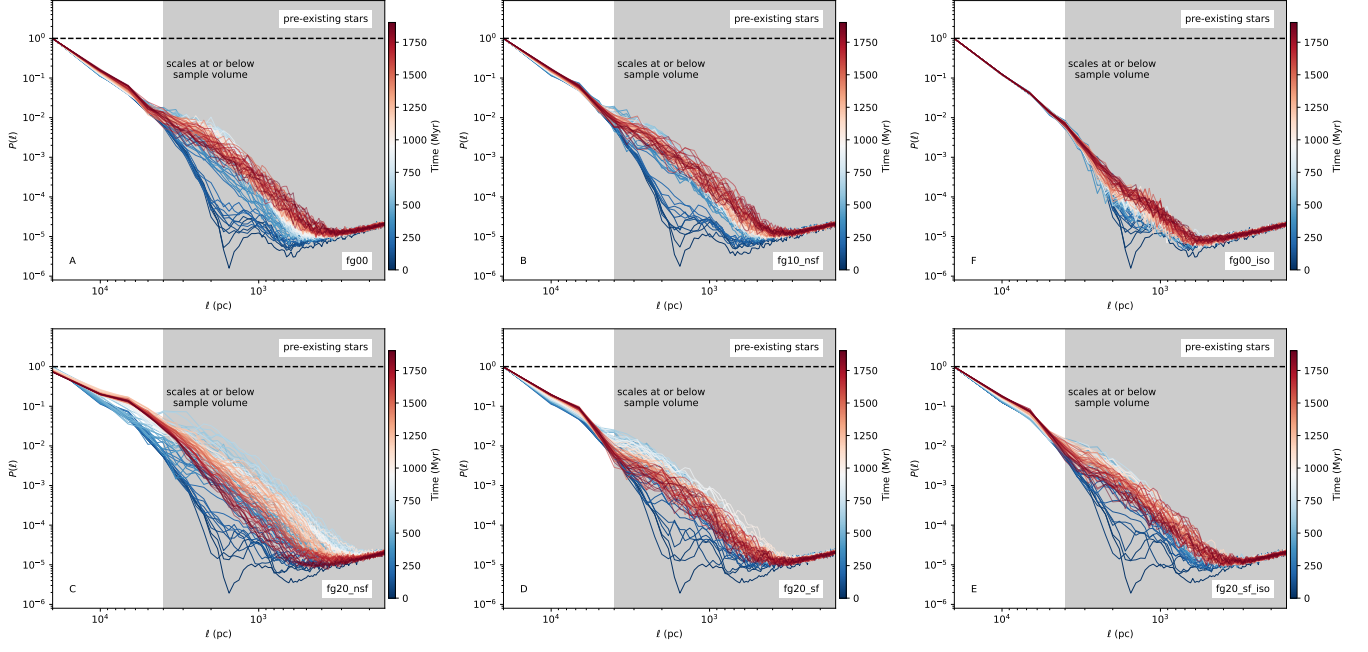


**Figure B1.** Similar to Fig. 8, but for the distribution of pre-existing stars. The  $P(\ell) \propto \ell^2$  behaviour at the smallest scales is a reflection of the particle (discretisation) noise.

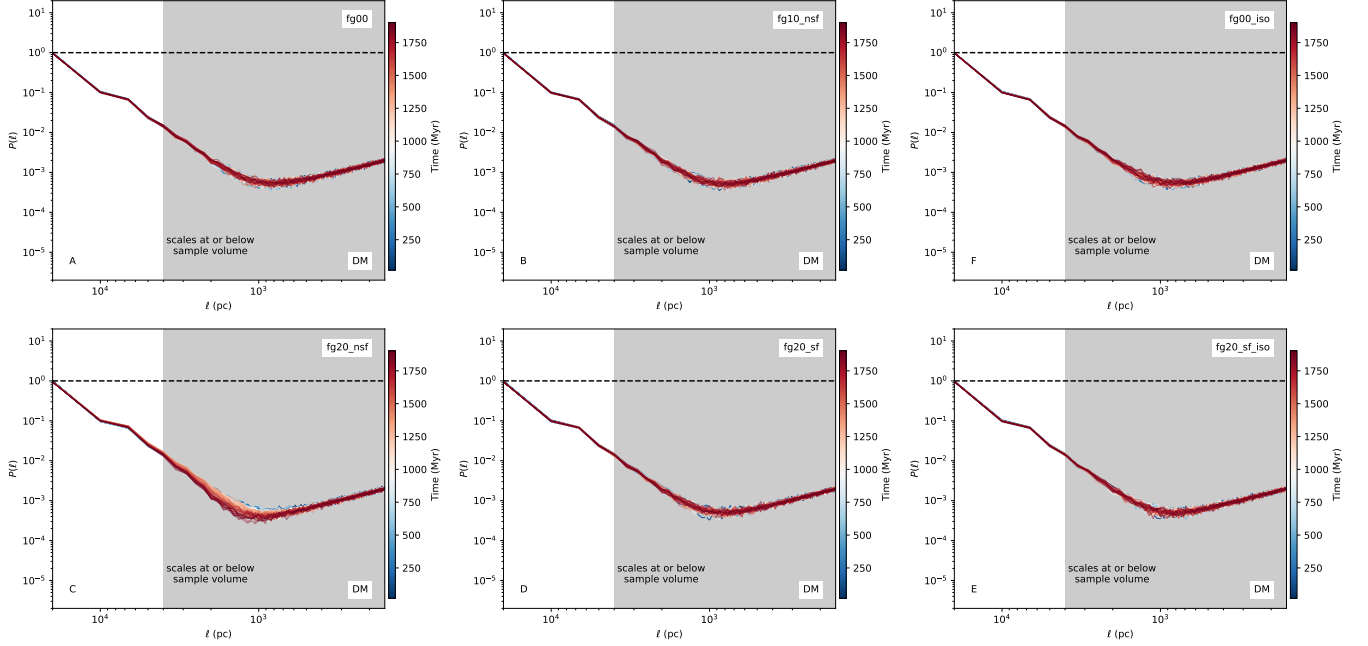


**Figure B2.** Similar to Fig. B1, but for the mass distribution of dark matter.

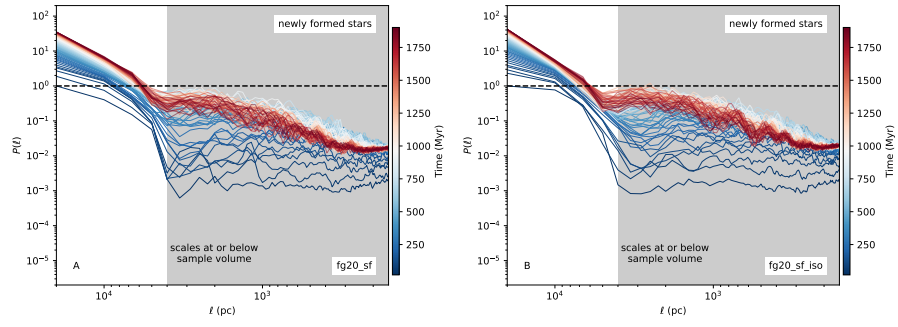


**Figure B3.** Similar to Fig. B1, but for the mass distribution of newly formed stars.